Data assimilation techniques for plasma dynamics and chemistry for electric propulsion systems

IEPC-2024-710

Presented at the 38th International Electric Propulsion Conference, Toulouse, France
June 23-28, 2024

Kentaro Hara*
Aeronautics and Astronautics, Stanford University, Stanford, CA, 94305, USA

While physics-based models, including kinetic, fluid, and hybrid approaches, remain important computer simulation tools, an alternative is to use data-driven models. In data assimilation, the key idea is to combine the estimates of state variables and parameters obtained from a physics-based dynamical model with noisy experimental data. This approach is often called model-data fusion. In recent years, we have developed data assimilation techniques using variants of Kalman filters, which has been often used in the controls, robotics, and weather forecasting communities. Here, we demonstrate the data assimilation techniques for several different test cases, including Lorenz attractor problem, electron temperature of predator-prey model, plasma chemistry and pulsed plasma systems, electron mobility estimation from Hall effect thrusters.

I. Introduction

Various electric propulsion (EP) devices have been developed over the past few decades and now the EP technology has matured to a level that it transitioned into industry. Looking at the success of the aeronautical industry, development of computational models plays an important role especially starting around late 1960s when computational fluid dynamics (CFD) became available. With a few decades of academic and industrial research, CFD is now the main driver of the aeronautical industry to design aircraft and their components minimizing the amount of prototypes and experimental testing required. Therefore, while experimental diagnostics and measurements are always required to guarantee safety and performance with some reliability, the need of high-fidelity and cost effective computational models exponentially increases when the engineering product becomes more mature.

For theoretical and computational models, there are generally physics-based and data-driven models. Physics-based models do not require data (i.e., experimental data) within the computational model. Hence, the governing equations with certain assumptions are solved in time and space. The results obtained from such a physics-based models can be compared with analytical (exact) solutions for verification and experimental data for validation. Sometimes, comparing a simulation result obtained from a particular code with results obtained from a different code is also called validation, but we will call this approach benchmarking. Once the computational models are developed, one can also study the computational performance (i.e., scalability, CPU hour, optimization, etc). On the other hand, there are data-driven models. Broadly speaking, there are data-driven models that do not rely on a dynamical model (e.g., physics-based models) and there are ones that couple a dynamical model with experimental data. For instance, neural network can be considered as providing an input-output correlation map without the need to discuss what the underlying physical processes are involved. There are more state-of-the-art models that incorporate physics into the neural network and machine learning (ML) techniques, such as physics-informed neural network (PINN). However, the physics is taken into account as a constraint rather than some underlying dynamical model to increase the interpretability of the outputs obtained from the neural network.

One of the promising data-driven models that could have the biggest impact to engineering is the data-driven models that respect the underlying physics-based models and couple with incoming experimental

---

[*] Assistant Professor, Aeronautics and Astronautics, kenhara@stanford.edu.

data. Due to its coupling between a dynamical model and experimental data, this technique is also called model-data fusion or data assimilation. Generally speaking, data assimilation is conducted via the following strategies. One, the physics-based model provides an estimate of the state variables. Second, when the measurement data are acquired, the estimated state variables are updated. Such state estimation methods are developed using a statistical approach.

Over the past few years, we have developed several data-driven models using extended Kalman filter (EKF) and recently using ensemble Kalman filter (EnKF). The basic idea, numerical model formulation, and test cases are discussed in this paper.

II. Statistical perspective behind state estimation

Figure 1 shows the basic statistical concepts for state estimation techniques. A state variable (here in the figure, is the position of the vehicle in the x direction) is *estimated*. There is an uncertainty in us knowing the exact position of the vehicle. Thus, the vehicle position can be described using a probably density function (PDF). For instance, the vehicle starts at the $x = x_{t-1}$, where t here denotes a time step. Initially, the exact position of the vehicle may be $x = x_{t-1} \pm \sigma R$, where σ is the width of the PDF, such as the standard deviation, and R is a random number. Thus, in general, one can consider x to a random variable (or in other words an uncertain variable) that is described by a PDF, i.e., $PDF = F(x)$. Hence, if one takes the moments of this PDF (similar to gas kinetic theory), the mean value of the PDF can be written as $\hat{x} = \int xF(x)dx$. The second moment lead to the covarance or variance $P = \int(x-\hat{x})^2F(x)dx$, which is similar to the temperature in gas dynamics.

The key idea of data assimilation is that the initially uncertain state variables propagate in time (and space) with some underlying nonlinear (can be linear) dynamics. Thus, the initial $F(x, t-1)$ at $t-1$ time step can be updated using the physical model to the next time step t. Depending on the nonlinear dynamics of the physical processes of interest, the PDF can changes its values and shape. One could completely trust the nonlinear dynamical model, but any mathematical governing equation is an approximation to the ground truth because there might be some terms that are missing and/or there are other effects (e.g., external disturbance) that are not accounted for in the governing equations that one chooses to use. Hence, one considers that there is an uncertainty associated with how well we know the dynamical model. This is called the process noise. With the process noise in the dynamical model, the initial PDF can be updated to the PDF at t, i.e., $F(x, t)$. When the vehicle moves, the most probably (i.e., mean) estimate of the vehicle position moves but at the same time its uncertainty can also increase or decrease. An example of this is that at the initial condition, we may consider that the vehicle is at $x = 0$ m, but after 1 hour, $x = 60$ mile. If we have the process noise (which we typically consider), the model may predict that the vehicle position needs to be at $x = 60$ mile with a 3% uncertainty, i.e., the vehicle may be at $x = 57.2 - 61.8$ mile. This is described using the blue line, which shows x_t^{pred} in the figure.

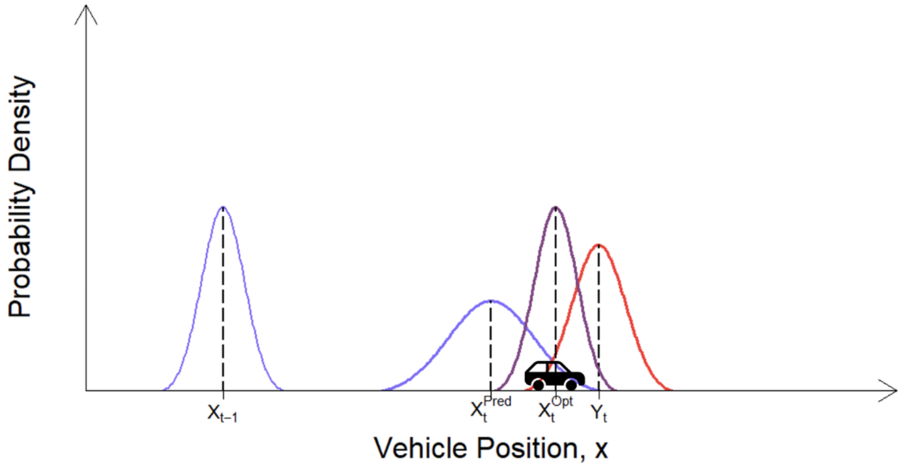

Figure 1. Statistical approach for Kalman filters. Taken from `https://www.lancaster.ac.uk/stor-i-student-sites/jack-trainer/how-nasa-used-the-kalman-filter-in-the-apollo-program/`

An important concept behind state estimation is that the measurement data are available, which is described using $y(t)$. Often times, the measurement quality is dependent on the measurement itself. For instance, what is the resolution in space and time and was there any external perturbations on to the diagnostics? All such uncertainties can be now considered as the measurement noise. Typically, the users (i.e., the diagnostician) knows the error bars in their measurement data. Another interesting connection between the dynamics and the measurements is that the measurement data can be described using some state variables that are estimated from the physics-based dynamical model, i.e., the measurement data is a function of the state variables. With the measurement noise, there is a PDF of the measurement data as well. For instance, the camera at $t = 1$ hour, may suggest that the vehicle position is at $x = 62$ mile with a 2 % uncertainty.

Kalman filter is an approach to use the PDF of the estimated state variable and the PDF of the measurement data to infer what the *optimal* estimate is. Using the two PDFs, the Kalman filter might tell the user that the most optimal estimate is $x = 61$ mile with at 1.5 % uncertainty. Hence, the estimate after the measurement update is assigned a new mean value $\hat{x}$ and covariance P. The mathematical model for Kalman filter is given in the next section.

III. Kalman filter model

The dynamical model of interest can be generally written as

$$\frac{d\mathbf{x}}{dt} = f[\mathbf{x}(t)] + \mathbf{w}, \tag{1}$$

where $\mathbf{x}$ is the state vector, i.e., vector of state variables, f is the function that provides the dynamics of how the state varies in time, and $\mathbf{w}$ is the process noise, which is conceptually the uncertainty between the dynamical model and the ground truth. The measurement data can be described as

$$\mathbf{y} = h(\mathbf{x}) + \mathbf{v}, \tag{2}$$

where $\mathbf{y}$ the vector of measurement data, which can be multimodal or can describe measurements at different spatial location, h is the function that provides how the measurement data can be described using the state variables (cf. nonlinear observer model), and $\mathbf{v}$ is the measurement noise.

A. Difference between extended Kalman fitler and ensemble Kalman filter

Figure 2 shows the difference between extend Kalman filter (EKF) and ensemble Kalman filter (EnKF). All filtering techniques basically propagate and update the PDFs of the state variables. Here, t_k is the time at which measurement data acquisition takes place. In the EKF, the mean value of PDF, $\hat{\mathbf{x}} = \int \mathbf{x}F(\mathbf{x})d\mathbf{x}$, and covariance, $P = \int(\mathbf{x} - \hat{\mathbf{x}})(\mathbf{x} - \hat{\mathbf{x}})^T F(\mathbf{x})d\mathbf{x}$, are predicted by the dynamical model and updated using measurement data. Here, if $\mathbf{x}$ is a vector with size of $n \times 1$, P is a $n \times n$ matrix. It can be seen that superscript $-$ and $+$ denote the estimates before and after the measurement update, respectively. The EnKF is a different approach as some ensembles (different $\mathbf{x}$ values) are considered at a time step. The number of ensembles is denoted using N. Hence, the mean value of PDF is approximated as $\hat{\mathbf{x}} = N^{-1}\sum_{i=1}^{N}\mathbf{x}_i$ and the covariance is given by $P = N^{-1}\sum_{i=1}^{N}(\mathbf{x}_i - \hat{\mathbf{x}})(\mathbf{x}_i - \hat{\mathbf{x}})^T$. It is to be noted that in EnKF, the calculation of the mean and covariance is only required at the Kalman update phase, when the data assimilation takes place. Thus, EnKF can be computationally more efficient than EKF that requires the time-dependent calculation of the $n \times n$ size covariance matrix.

B. Extend Kalman filter: model

Here we describe how the EKF works. First, initial estimates for the augmented state vector $\hat{\mathbf{x}}_0 = \hat{\mathbf{x}}(t = 0)$ and the error covariance matrix $P_0 := P(t = 0)$ are chosen. Next, for each time step that we obtain the data, we perform the following sub-steps until all time samples have been utilized.

Prediction: Predict the state variables that includes parameters, $\hat{\mathbf{x}}$, and their covariances, P, until the time when measurement data set arrives. Here, superscripts $+$ and $-$ denote the estimates after and before the measurement update. The physics-based model is employed between t_{k-1}^{+} and t_{k}^{-}, where k denotes the

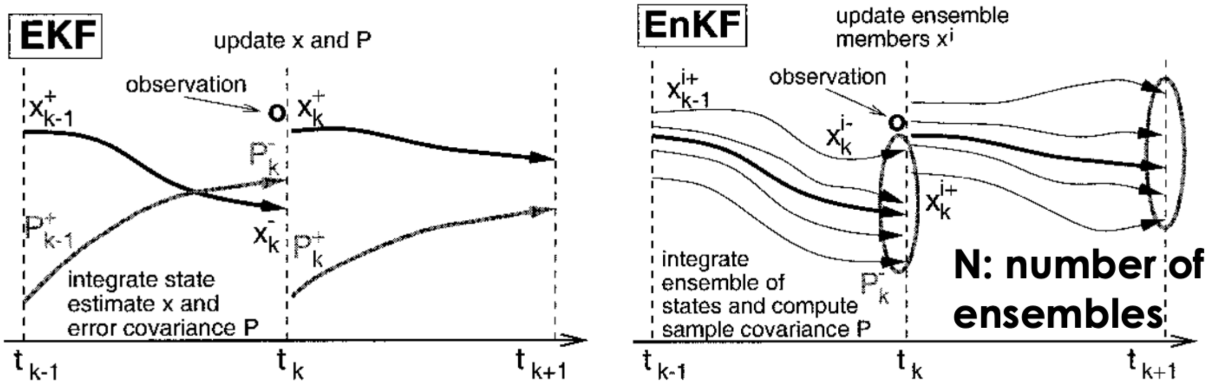

Figure 2. Comparison between (a) extended Kalman filter (EKF) and (b) ensemble Kalman filter (EnKF). Reproduced from Ref. 1

time step at which measurements are obtained:

$$\begin{aligned} \frac{d\hat{\mathbf{x}}}{dt} &= \mathbf{f}(\hat{\mathbf{x}}, t), \\ \frac{dP}{dt} &= LP + PL^T + Q(t), \end{aligned} \tag{3}$$

where L is the Jacobian matrix of $\mathbf{f}$ evaluated at $\hat{\mathbf{x}}$ as shown in equation (1) and $Q(t)$ is the process noise covariance matrix. Assuming that process noise is uncorrelated in time, i.e., white noise, Q can be given as

$$E[\mathbf{w}(t)\mathbf{w}^T(t-\tau)] = Q(t)\delta(t-\tau), \tag{4}$$

where E is the expectation and τ is a time delay. The delta function denotes that the process noise is not correlated in time.

Update: Update the state and covariance estimates when a measurement is acquired, i.e., at k-th time step:

$$\begin{aligned} &\hat{\mathbf{x}}^+_k = \hat{\mathbf{x}}^-_k + K_k[\mathbf{y}_k - h(\hat{\mathbf{x}}^-_k)], \\ &P^+_k = (I - K_k H_k)P^-_k, \end{aligned} \tag{5}$$

where $H_k = \frac{\partial}{\partial \mathbf{x}} h(\mathbf{x})\big|_{\mathbf{x}=\hat{\mathbf{x}}^-_k}$ is the Jacobian of the measurement function, I is the identity matrix,

$$K_k = P^-_k H^T_k (H_k P^-_k H^T_k + R_k)^{-1} \tag{6}$$

is the Kalman gain, and R is the measurement noise covariance matrix. Here, the measurement noise covariance is defined as

$$E[\mathbf{v}(t)\mathbf{v}^T(t-\tau)] = R(t)\delta(t-\tau), \tag{7}$$

C. Physics-constrained EKF

In Ref. 2, it was realized that the choice of Q and R can cause the simulation to fail because the variance, i.e., diagonal terms of P, becomes negative, which is not mathematically correct. As Q is the process noise covariance, the direct determination of the values is impractical. On the other hand, from an engineering point of view, the measurement noise covariance R is more practical because any diagnostic tools are associated with some experimental / measurement errors. For instance, a Langmuir probe in the ion saturation regime may result in the ion density to be within 50 %.

It was identified in Ref. 2 that the negative variance is calculated in the Kalman update, i.e., Eq. (5). For instance, if $H_k = [1, 0, 0, 0]^T$ and $\mathbf{x} = [x_1, x_2, x_3, x_4]^T$ is the state variable vector, the variance of the state variable x_4 can be written as

$$P^+_{44} = P^-_{44} - \frac{P^-_{14}P^-_{41}}{R + P^-_{11}}. \tag{8}$$

This equation shows that the variance corrected by the measurement is always smaller than the predicted variance. This may cause $P_{44}^{+} < 0$, which is not physically and mathematically correct. Hence, in the physics-constrained EKF, we set the diagnoal terms of the covariance matrix, P, to be always positive by adjusting Q or R.

Figure 3 shows the root-mean-square error of the time-averaged parameter in a Lorenz problem, obtained from 15 separate runs for the PC-EKF (circle) and the original EKF (diamond). The EKF solutions are not shown below a measurement frequency of 5 since a finite number of runs failed, while the PC-EKF exhibits robust state estimation with sparse data.

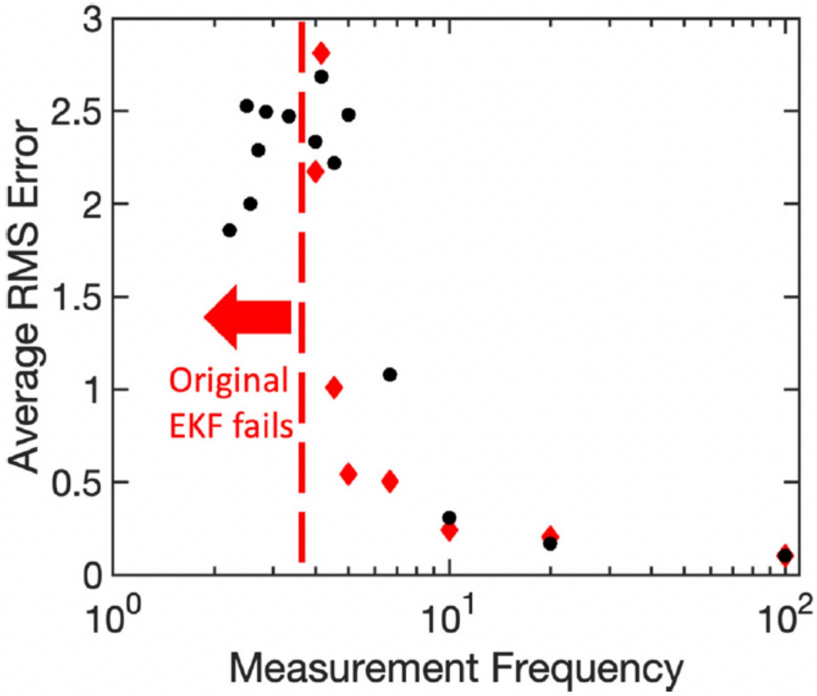

Figure 3. Physics-constrained EKF vs. regular EKF with constant Q and R. Reproduced from Ref. 2.

IV. Results

So far, we have developed an EKF for plasma dynamics. The key idea for the data assimilation is to use experimental data to infer the hidden properties that are difficult to measure. Hence, we adopt a step-by-step approach in increasing the fidelity of the data assimilation technique.

A. Hall effect thruster (HET)

HETs are known to operate with a wide range of oscillations, from 1 kHz to 10 MHz. Some oscillations include loop oscillations, circuit oscillations, breathing mode oscillations, ion transit oscillations, ion acoustic waves, and rotating spokes. This indicates that not only the plasma properties but also the transport and rate coefficients, which we can consider to be a *parameter* than the state variables themselves, are varying in space and time. Measurements such parameters at high frequency (e.g., above 1 MHz) can be extremely challenging due to the available diagnostic techniques as well as the spatial and temporal resolution of the measurements.

1. *Greve et al. 2021*

First, we demonstrated the EKF approach using a 0D plasma global model. We consider the following dynamical model:

$$\frac{\partial N_i}{\partial t} + \frac{N_i U_i}{L} = N_i N_n k_{ion}, \tag{9}$$

$$\frac{\partial N_n}{\partial t} + \frac{(N_n - N_{inj})U_n}{L} = -N_i N_n k_{ion}, \tag{10}$$

where N_i and N_n are the ion and neutral atom densities, U_i and U_n are the ion and neutral atom bulk velocities, L is the plasma lengths, N_{inj} is the neutral atom density that corresponds to the injection, and k_{ion} is the ionization rate coefficient. Here, the ionization rate coefficient is a function of electron temperature:

$$k_{ion}(T_e) = \left[A T_e^2 + B \exp\left(-\frac{C}{T_e}\right)\right] \left(\frac{8 k_B T_e}{\pi m_e}\right)^{1/2}, \tag{11}$$

where $A = -1 \times 10^{-24}$, $B = 6.386 \times 10^{-20}$, $C = 12.13$, k_B is the Boltzmann constant, m_e is the electron mass.[?]

Figure 4 shows the data assimilation using a SPT-100 thruster data in Ref. 3. The discharge current, shown in Fig. 4(a1,b1), is reconstructed into a time-dependent ion density, which is considered to be the measurement data for the EKF (see black dashed line in Fig. 4(a2,b2)). Thus, $y = N_i$. The state vector for the EKF-0D global model is $\mathbf{x} = [N_i, N_n, T_e]^T$. As the electron temperature is considered to be a parameter in this present study, $dT_e/dt = 0$, i.e., the dynamics of the electron temperature is not known. As the measurement updates are performed, N_i, N_n, and T_e are all updated. Hence, the time-dependent estimation of T_e, as shown in Figs. 4(a4,b4), is solely from the Kalman update, shown in Eq. (5). The results indicate that the EKF coupled with a 0D global model can be used to infer a time-dependent parameter without knowing the dynamics of the parameter.

2. *Troyetsky et al. 2023*

In Ref. 2, there were 2 equations and 2 state variables with 1 parameter. This work was extended by Troyetsky et al. to include more physics into the dynamical model, allowing for estimation of a different parameter.

In addition to Eqs. (9) and (10), the electron energy equation is now included:

$$\frac{\partial}{\partial t}\left(\frac{3}{2} N_i k_B T_e\right) + \frac{5}{2}\frac{N_i U_e T_e}{L} = S_j - S_w - S_c, \tag{12}$$

where $S_j = -N_i U_e E$ is the electron energy input due to Joule heating, U_e is the electron axial bulk velocity, $E \approx V_d/L$ is the electric field, $S_w = N_i \epsilon_w \nu_w$ is the electron energy loss due to the walls, $S_c = \chi N_i N_n k_{ion} \Delta\epsilon_{ion}$ is the electron energy loss due to inelastic collisions, χ is the ionization cost, $\Delta\epsilon_{ion}$ is the ionization energy. Here, $\nu_w = \sqrt{k_b T_e/m_i}/(1-\sigma)/R_\Delta$ is the wall collision frequency, where R_Δ is the channel width, m_i is the ion mass, and σ is the effective secondary electron emission rate. In addition, $\epsilon_w = 2k_B T_e + (1-\sigma)\phi_w$ is the electron energy loss to the wall, where ϕ_w is the sheath potential.

The discharge current can be approximated as

$$I_d = e A_c N_i (U_i - U_e), \tag{13}$$

where A_c is the channel area. Here, there are 3 equations (ion continuity, neutral continuity, and electron temperature), 3 state variables (ion density, neutral density, adn electron temperature), and 1 parameter (electron bulk velocity). The discharge current data are obtained using a Rogowski coil at a sampling rate of 100 MHz for a 1.5 kW laboratory HET model.

Figure 5 shows the results of the EKF, including the time histroy of estimated states, power spectral density (PSDs), and phases with respect to the discharge current for the thruster operating at 100 V. It can be seen that the dominant frequency is 6 kHz. In Fig. 5(a1-e1), the black curves for the time histories are smoothed using a 100 datapoint running average to visualize the data without the high-frequency signals. The maximum peak-to-peak oscillation amplitudes, normalized by the mean values of each state, are 10%, 2%, 2%, and 48%, for N_i, N_n, T_e, and U_e, respectively.

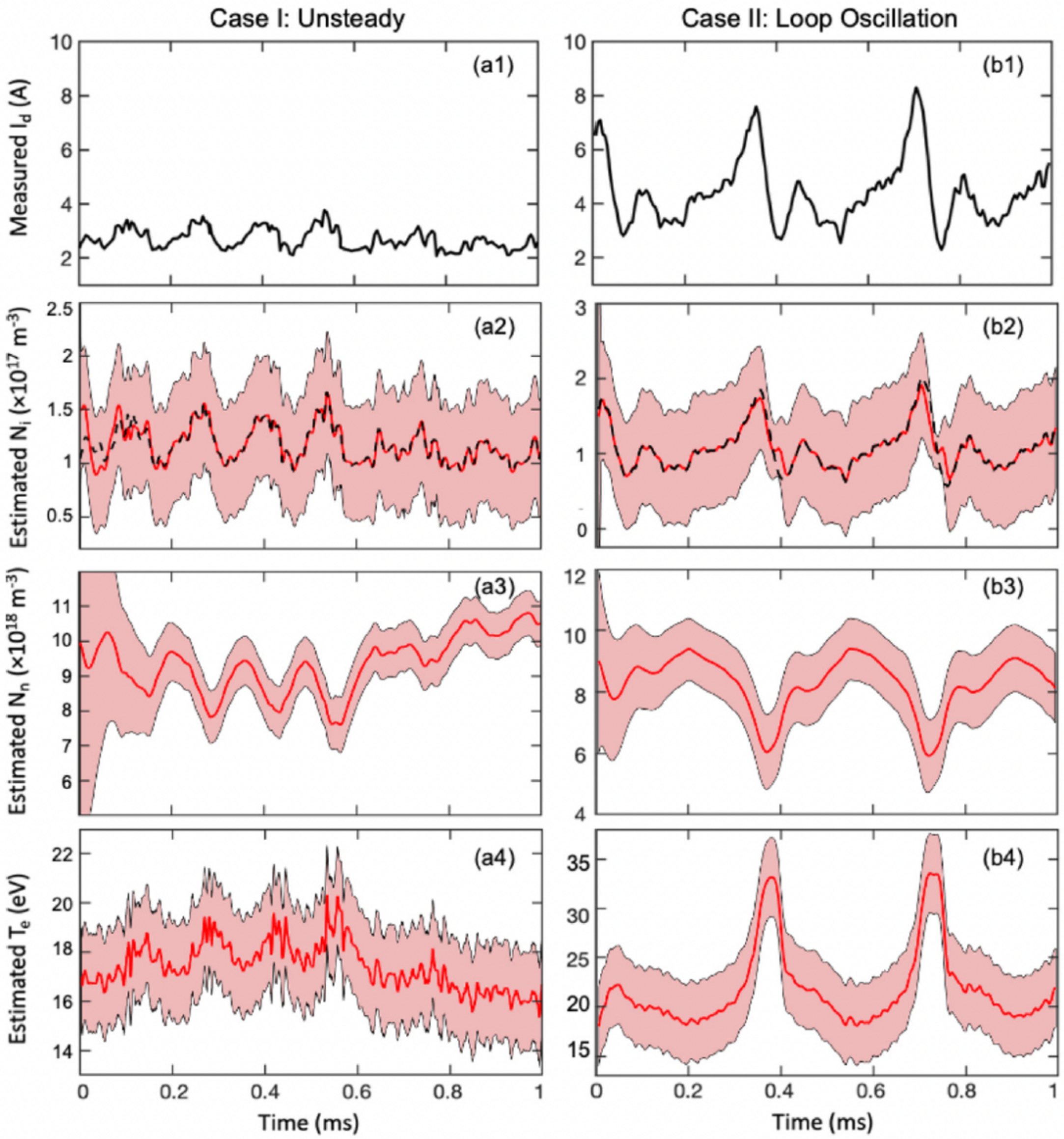

Figure 4. Results obtained from the physics-constrained EKF using the 0D ionization oscillation model for various Hall effect thruster operation. (a) 70 V discharge voltage and (b) 125 V discharge voltage for a SPT-100. The experimental data are obtained from Ref. 3. The measurement discharge current [(a1) and (b1)], estimated ion number density [(a2) and (b2)], estimated neutral number density [(a3) and (b3)], and estimated electron temperature [(a4) and (b4)] are shown. Reproduced from Ref. 2.

Figures 5(a2)–(e2) show the PSDs of the discharge current, estimated ion number density, neutral number density, electron temperature, and electron bulk velocity, respectively. The gray curves show the non-smoothed data and the black curves show the data smoothed with a 10 point running average to better visualize the dominant modes. In all PSDs, there is a dominant frequency at 6 kHz, with at least the first harmonic at 12 kHz also prominent in all states other than U_e.

Figures 5(b3)–(e3) show the phases of the estimated states relative to the discharge current. The phases calculated using the FFT analysis of the EKF estimates are shown in gray and the analytical phases are shown in blue. The purple diamond shows the location of the dominant oscillation, in this case at 6 kHz. In the low frequency limit, the fluctuations of N_i and T_e are in phase with the discharge current oscillations, whereas those of N_n and U_e are 180° out of phase. Near the dominant oscillation frequency, the phase of N_i is 67°, while the phases of N_n, T_e, and U_e are all within 10° of their asymptotic values (180° for N_n and

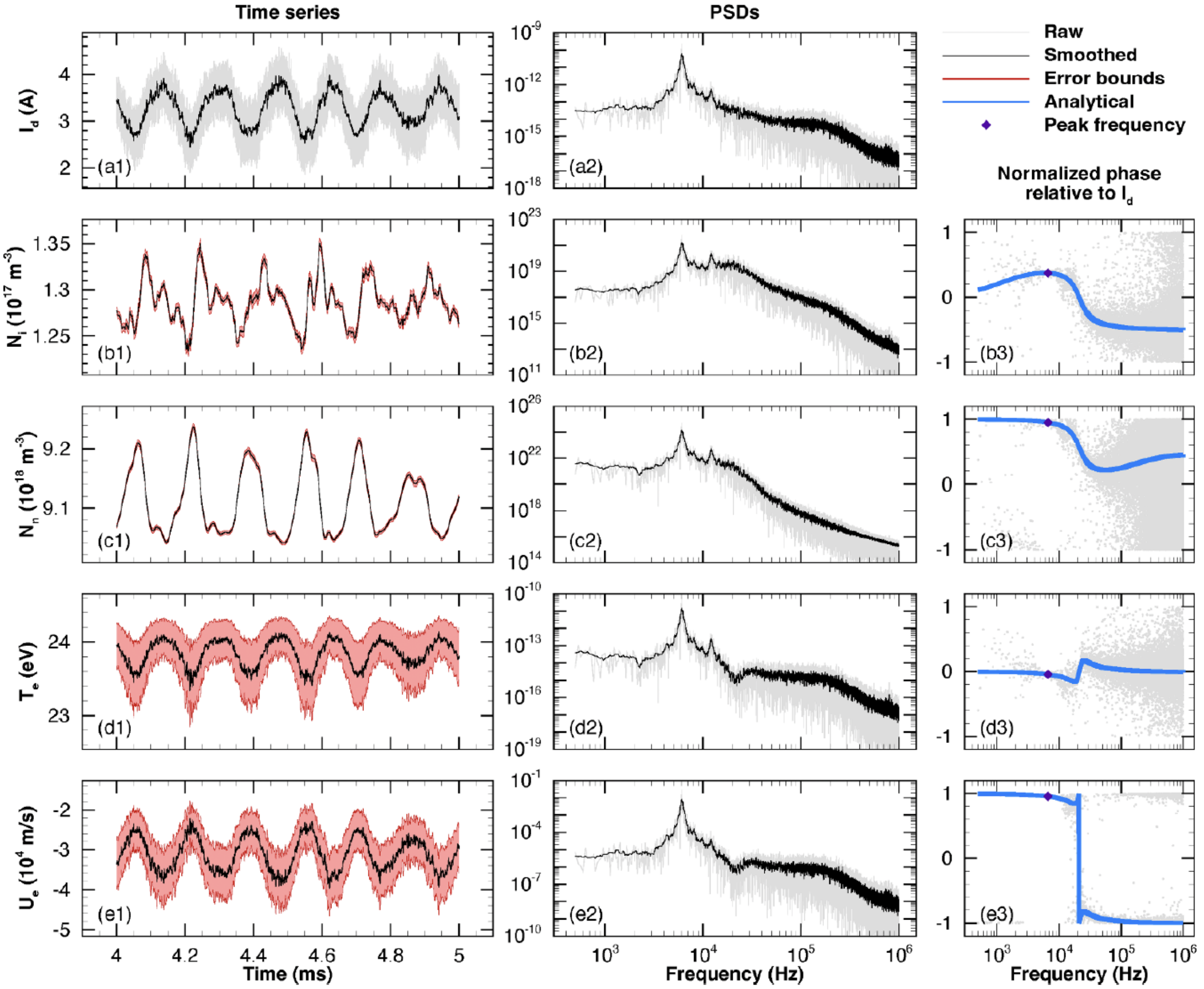

Figure 5. EKF estimates for the 100 V dataset from a Hall effect thruster. The top two panels show the discharge current (a1) signal estimate and (a2) PSD. (b1)–(e1) The smoothed state estimates (black) and 3σ error bounds (pink) for each state. (b2)–(e2) The state PSDs, both raw (gray) and smoothed (black). (b3)–(e3) The phase lag of each state relative to I_d as obtained from the FFT (gray) and phase analysis (blue). The frequency of the dominant peak from the PSD (6 kHz) is shown with a purple diamond. Smoothing is done with a running window of 100 points for time data and 10 points for frequency data. An increase in noise in the phase estimates can be seen beginning at higher frequencies. Reproduced from Ref. 4.

U_e, and 0° for T_e).

The main reason why the electron temperature equation is added is because now U_e can be inferred from the DA approach. This allows for the estimation of cross-field electron transport as given as,

$$\mu_\perp = -\frac{U_e}{E}, \tag{14}$$

where E is the electric field. Here, due to the 0D approximation, the diffusion flux is considered to be negligible, i.e., the drift flux carries the electron current. The electron-neutral momentum transfer collision frequency is given as $\nu_c = \nu_m + \nu_w + \nu_{ei}$, where ν_m is the elastic and inelastic collision contribution to the electron momentum transfer and ν_{ei} is the electron-ion Coulomb collision frequency. The anomalous electron transport frequency is calculated as

$$\nu_a = -\frac{eB^2 U_e}{m_e E} - \nu_c, \tag{15}$$

which is obtained by assuming the cross-field electron mobility in the limit of large Hall parameter $\Omega = \omega_B/\nu_{eff}$, where ν_{eff} includes the classical collision frequency and the anomalous electron transport frequency.

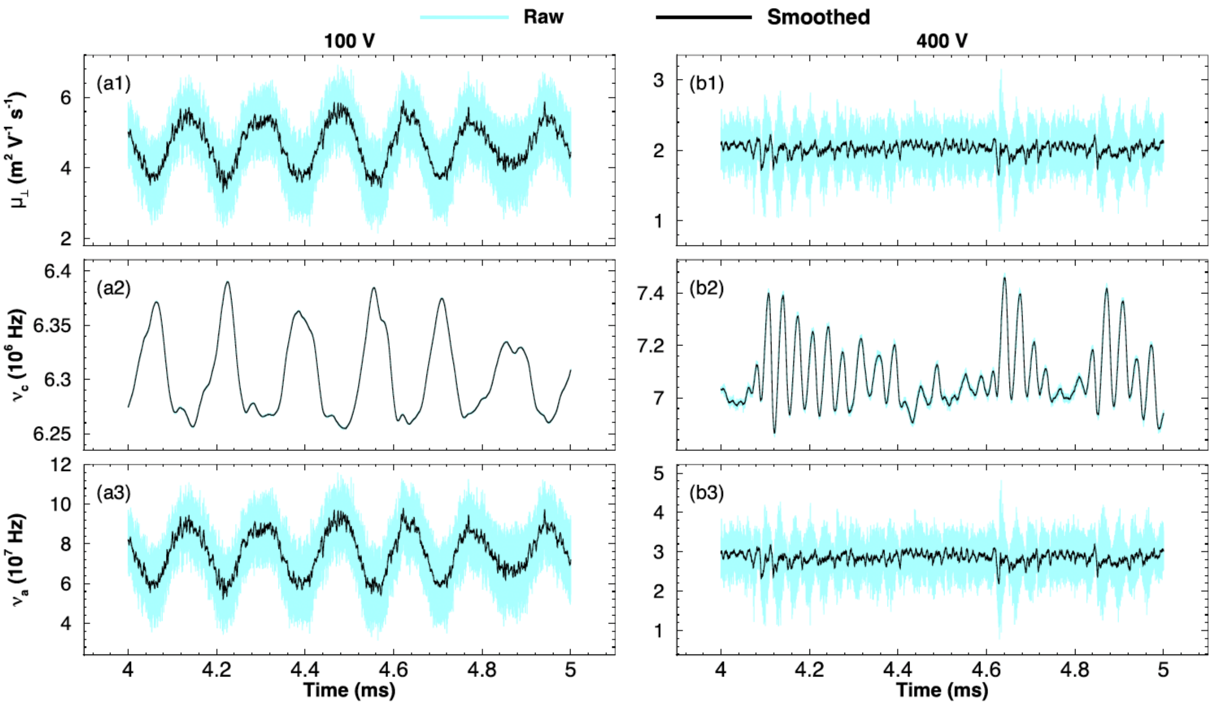

Figure 6. The estimates of the cross-field electron mobility, classical collision frequency, and anomalous electron transport frequency. Reproduced from Ref. 4.

Figure 6 shows the estimates of the time-dependent cross-field electron transport. Due to the oscillations in U_e for different discharge conditions, i.e., $V_d = 100$ V and 400 V, the time dependent electron mobility and anomalous electron transport frequency are estimated differently. At 100 V and 400 V, the time-averaged electron mobilities are 4.7 m^2 V^{-1} s^{-1} and 2.0 m^2 V^{-1} s^{-1}, with maximum fluctuations of approximately 35% and 15% of their mean values, respectively.

B. Pulsed inductively coupled plasma: Greve et al. 2022

Here, the main interest is in utilizing the EKF with a 0D plasma global model to capture some plasma chemistry effects, e.g., rate coefficients, radiative transport, and surface effects. For this research, the dynamical model of interest is the 0D plasma global model. The rate equations are given by

$$\frac{dN_j}{dt} = S_{source,j} - S_{sink,j}, \tag{16}$$

where $S_{source,j}$ and $S_{sink,j}$ are the source and sink terms for species j. The source and sink are a function of the number densities of the relevant species as well as the rate coefficient which is a function of electron temperature, assuming a Maxwellian electron energy distribution function. The other equation we need is the electron energy equation:

$$\frac{d}{dt}\left(\frac{3}{2}n_e k_B T_e\right) = \frac{P_{abs}}{V} - S_{elas} - S_{inelas}, \tag{17}$$

where n_e is the electron density, P_{abs} is the electron power absorption, V is the volume of the discharge, S_{elas} is the energy loss due to electron elastic collisions, and S_{inelas} is the energy loss due to electron inelastic collisions, including excitation and ionization. Typically, the electron power absorption for RF systems is difficult to measure, because the power that can be measured is in the circuit level, i.e., electrical power that is equal to current times voltage.

Figure 7 shows the application of EKF using the plasma global model for an argon pulsed inductively coupled plasma. The measurements are taken from literature, which studied the effects of duty cycle,

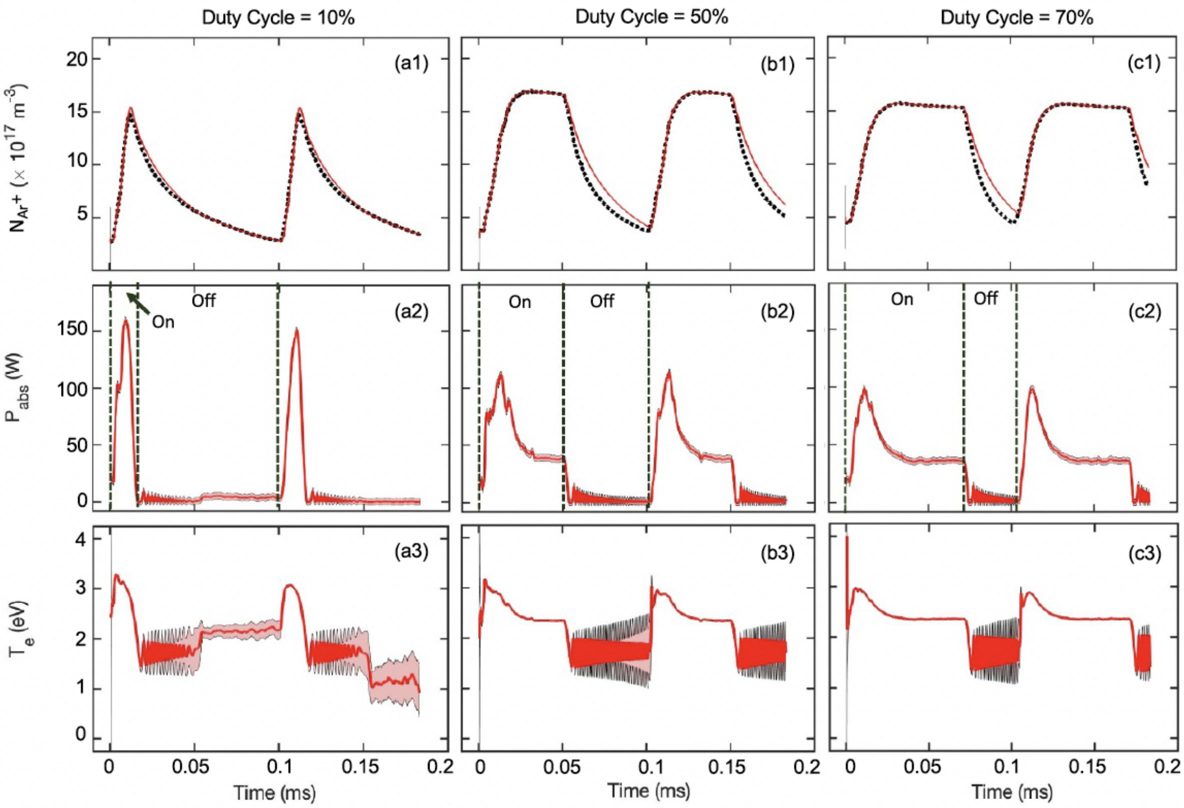

Figure 7. The effect of the duty cycle on the pulsed plasma dynamics. Here, duty cycles of (a) 10%, (b) 50%, and (c) 70% are studied based on experimental data from Ref. 5 with a peak power of 300 W and a pulse frequency of 10 kHz. (1) The ion number density measurements (black dashed line) compared to the estimated values (red solid line), (2) the corresponding absorbed electron power estimates with their 3σ uncertainty bounds (pink shade), and (3) the electron temperature estimates and their 3σ uncertainty bounds. Reproduced from Ref. 6.

frequency, and power on the pulsed operation. Here, the ion (i.e., electron) plasma density is the measurement and the electron power absorption is the parameter that is estimated. It can be seen that the duty cycle of the pulsed operation, i.e., power on and off phases, are correctly estimated without the model *a priori* knowing the pulsed cycle.

V. Summary

We have developed extended and ensemble Kalman filter for plasma physics and chemistry applications. The data assimilation techniques are useful to estimate and infer the parameters and state variables that cannot be easily measured. The filtering approach is essentially solving an inverse problem time dependently, allowing for a time-dependent estimation of the state and parameters.

Acknowledgements

The contributions from Christine Greve (currently at Air Force Research Laboratory), Daniel Troyetsky (currently a PhD student at Stanford University), and Anubhav Dwivedi (currently a postdoc at Stanford University), are appreciated. I also acknowledge the work conducted by Mathieu Cerepi and Theo Zivre, who were master's students at Stanford University. This work was supported by NASA through the Joint Advanced Propulsion Institute, a NASA Space Technology Research Institute under Grant No. 80NSSC21K1118, the Air Force Office of Scientific Re- search under Awards and No. FA9550-21-1-0433, and Global Research Outreach program of Samsung Mecha- tronics Research.

References

[1] R. H. Reichle, J. P. Walker, R. D. Koster, and P. R. Houser, "Extended versus ensemble kalman filtering for land data assimilation," *Journal of Hydrometeorology*, vol. 3, no. 6, pp. 728 – 740, 2002.

[2] C. M. Greve, M. Majji, and K. Hara, "Real-time state estimation of low-frequency plasma oscillations in Hall effect thrusters," *Physics of Plasmas*, vol. 28, p. 093509, 09 2021.

[3] N. Gascon, M. Dudeck, and S. Barral, "Wall material effects in stationary plasma thrusters. I. Parametric studies of an SPT-100," *Physics of Plasmas*, vol. 10, pp. 4123–4136, 10 2003.

[4] D. E. Troyetsky, C. M. Greve, S. Tsikata, and K. Hara, "State estimation of the dynamic behavior of plasma properties in a hall effect thruster discharge," *Journal of Physics D: Applied Physics*, vol. 56, p. 444001, aug 2023.

[5] G. A. Hebner and C. B. Fleddermann, "Characterization of pulse-modulated inductively coupled plasmas in argon and chlorine," *Journal of Applied Physics*, vol. 82, pp. 2814–2821, 09 1997.

[6] C. M. Greve and K. Hara, "Estimation of plasma properties using an extended kalman filter with plasma global models," *Journal of Physics D: Applied Physics*, vol. 55, p. 255201, mar 2022.